ARTICLES

Structures in classical phase space and quantum chaotic dynamics

B. S. Helmkamp and D. A. Browne
Department of Physics and Astronomy, Louisiana State University, Baton Rouge, Louisiana 70803-4001
(Received 21 October 1993)

We compare the quantum and classical dynamics of a particle moving in a cosine potential while subject to a time-dependent force. We concentrate here on the behavior of an initially well-localized wave packet at times before the classically chaotic motion is fully developed. We find that the quantum and classical dynamics are indistinguishable well beyond the Ehrenfest time where the wave packet delocalizes. The quantum and classical descriptions first differ precisely when the classical probability density is folded in the vicinity of a hyperbolic fixed point. At this point, the wave function acquires a nodal structure which we show to be the result of a simple beating phenomenon between paths in the semiclassical propagator.

PACS number(s): 05.45.+b, 03.65.Sq

I. INTRODUCTION

Although quantum mechanics contains classical mechanics as a limiting case, the quantum dynamics of a classically chaotic system does not show any obvious features that reflect the classical chaos [1]. The lack of sensitivity to initial conditions and the absence of mixing behavior at long times is often attributed to the linearity of Schrodinger equation as compared to the nonlinear Hamiltonian equations of motion. Resolving this apparent paradox is the central problem in understanding "quantum chaos."

Most studies of the quantum manifestations of classical chaos have focused on the energy domain for time-independent Hamiltonian systems. One quantum feature these systems exhibit is the non-Poissonian statistics of the energy-level spacings [2]. Integrable (regular) systems are characterized by the complete absence of level correlations and a Poisson distribution of level spacings. In contrast, nonintegrable (mixed) systems exhibit level repulsion in varying degrees while the energy levels for globally chaotic systems are strongly anticorrelated [3]. The other quantum feature seen in classically chaotic systems is the localization or "scarring" of eigenstates along classical periodic orbits [4]. Scars are intimately connected, in the semiclassical sense, to the marginally stable orbits of the underlying classical motion. Much of the recent literature is devoted to understanding these two phenomena.

Time-periodic Hamiltonians, like the one we discuss in this paper, have also received considerable attention. This is largely because the periodicity in time allows one to introduce quasistationary Floquet eigenstates and study the spectra of the Floquet eigenvalues [5]. This allows one to draw parallels to the presumably simpler time-independent systems with regard to phenomena like level correlations and scarring [6,7]. We do not use the Floquet formalism in this paper and focus instead on the behavior in the time domain because we are concerned with how the phase-space structures of classical chaos influence the quantum dynamics without any particular regard for symmetries of the Hamiltonian.

Our work is related to studies of the accuracy of semiclassical propagation in quantum systems at long times. Because the stationary-phase approximation used to derive the semiclassical propagator from Feynman's path integral formulation becomes invalid when the stationary paths coalesce at a caustic, Berry *et al.* [8] thought that the proliferation of caustics that characterizes chaotic dynamics must result in the early demise of semiclassical propagation. They characterized the classical motion via the deformation of curves in phase space. For motion dominated by an elliptic fixed point, a straight line in phase space develops into a "whorl," while unstable hyperbolic fixed points deform a straight line into "tendrils." By studying the length of time required to develop phase-space structure on a scale smaller than $\hbar$, they predicted that semiclassical propagation should fail much sooner for classical motion characterized by "tendrils" ($t_{\log} \propto \ln \hbar^{-1}$), than for classical motion characterized by "whorls" ($t \propto \hbar^{-1}$).

Tomsovic and Heller [9] demonstrated, however, that semiclassical propagation for classically chaotic conservative systems remains remarkably accurate well beyond these times. They have shown [10] that the quantum and semiclassical autocorrelation functions for wave packets initiated along chaotic trajectories of the stadium billiard are virtually identical well beyond $t_{\log}$. O'Connor and Tomsovic [11] observed similar long time accuracy in semiclassical propagation of the quantum baker's map. Sepulveda, Tomsovic, and Heller [12] reconcile these results with the work of Berry *et al.* by showing that the exponential proliferation of caustics in chaotic dynamics is accompanied by an exponential growth in the length of the tendrils such that the percentage of the total manifold which cannot be treated semiclassically grows linearly in-

stead of exponentially. Their analysis gives a time frame for the failure of semiclassical dynamics which scales as $\hbar^{-1/3}$ instead of $\ln \hbar^{-1}$.

In this paper we study the quantum, classical, and semiclassical evolution of a particle in a cosine potential also subject to a time-dependent force. We focus on the details of the dynamics at early times before the classically chaotic motion is fully developed. We pose this problem in the naive semiclassical limit where we can construct a well-localized wave packet to describe the initial state of the particle quantum mechanically and an equivalent localized classical probability distribution. Therefore we expect that the the quantum, classical, and semiclassical description of the dynamics to be very similar at short times. We study the differences between them in order to identify specific ways in which quantum effects inhibit the development of classical chaos.

Our analysis reveals three distinct times which define progressive stages in the development of the early-time quantum dynamics. The first time interval is characterized by a well localized wave packet and a compact classical probability distribution. In this regime the position and momentum operators in the Heisenberg equations of motion can be replaced by their mean (classical or quantum) values with no sensible error. This regime ends at the "Ehrenfest time" $t_{\rm Eh}$ where the second regime appears. Here both the quantum wave packet and the classical probability distribution spread out over a large fraction of phase space, but the two distributions remain essentially identical. The semiclassical behavior, however, has become tainted by caustics. The behavior in this time interval is controlled by the "whorls" associated with an elliptic fixed point. The first differences between the quantum and classical descriptions appear at the "equivalence time" $t_{\rm eq}$ and are associated with the development of tendrils in the classical phase-space distribution. These tendrils lead to a standing wave feature in the quantum distribution resulting from an interference between paths in the semiclassical propagator. There is also some additional structure that does not appear to have any semiclassical analog. On the other hand, if the classical probability density does not exhibit this folding, which is the case when the motion is regular, then the wave function does not acquire this nodal structure, and the quantum-classical equivalence persists within the time frame of our analysis.

In Sec. II we introduce the Hamiltonian we study and review earlier work on its classical behavior. Section III describes the calculational details of our study of the quantum, classical, and semiclassical evolution of the initial wave function. Our results are discussed in Sec. IV and our conclusions are contained in Sec. V.

II. THE PROBLEM

We study the Hamiltonian for particle of mass m in a periodic potential with wave vector k subject to a sinusoidally driven external force. The Hamiltonian is given by

$$H(p,x,t) = H_0(p,x) + V_t(x,t) \tag{1}$$

with H_0 the Hamiltonian for a classical pendulum whose frequency of small oscillations is Ω

$$H_0(p,x) = \frac{p^2}{2m} - \frac{m\Omega^2}{k^2}\cos(kx) \tag{2}$$

and the external driving force is described by

$$V_t(x,t) = -\epsilon x \sin \omega t. \tag{3}$$

This Hamiltonian is one of the simplest systems with sufficient complexity to exhibit classical chaos, and its classical behavior is fairly well understood [13]. It is also a good choice as a model Hamiltonian in describing the onset of classical chaos for systems which are made nonintegrable by a perturbation. The breakdown of integrability in this Hamiltonian occurs [14] because the perturbation produces traveling "resonances" that interfere with the primary orbit structure. The perturbation controls the amount of interference and thus the fraction of phase space filled with chaotic orbits.

For $\epsilon = 0$, the system is integrable and is confined to constant energy surfaces (orbits) which are the "invariant tori" in the language of Kolmogorov-Arnol'd-Moser (KAM) theory [15]. The bounded and unbounded motions are separated by a separatrix at zero energy. There are hyperbolic (unstable) fixed points on the separatrix at $p = 0$, $kx = (2n-1)\pi$ and elliptic (stable) fixed points at $p = 0$, $kx = 2n\pi$ where n is an integer. The phase-space structure for the unperturbed motion is shown in Fig. 1(a). For $\epsilon > 0$ but sufficiently small, the motion is still largely governed by a distorted version of the KAM tori, even though the motion is no longer confined to constant energy surfaces. The KAM structure breaks down in the immediate vicinity of the separatrix where

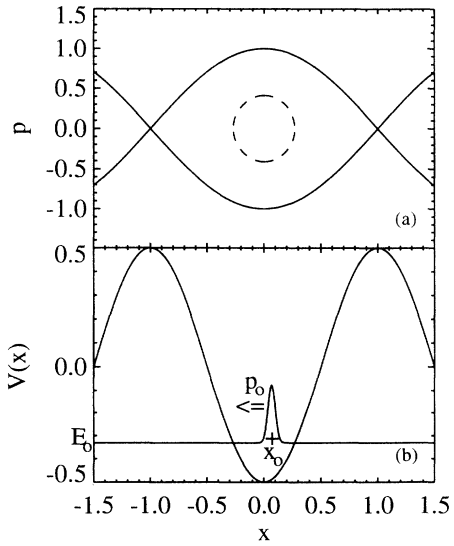

FIG. 1. (a) The unperturbed potential $V(x) = -(1/2)\cos(\pi x)$ with a schematic depiction of the initial wave packet centered at $x_0 = 0.067\,140$ with momentum $p_0 = -0.397\,000$. (b) The initial orbit (dashed) with $E = H_0(p_0, x_0) = -0.331$ and the unperturbed separatrix (solid) at $E = 0.500$.

the overlap of the resonances is strong, resulting in a stochastic layer which grows as ϵ is increased. For such resonance overlap to produce a large stochastic layer for small ϵ and lead to chaos, ω should be [13] comparable to the frequency of the unperturbed motion for orbits near but not in the stochastic layer. The trajectories that stay far from the stochastic layer remain bounded and regular, while those which get too close, particularly to the unstable fixed points, exhibit chaotic motion.

III. THE CALCULATIONS

We have chosen to use the same parameters for the unperturbed Hamiltonian as Lin and Reichl [13], $\Omega = k = \pi$, $m = 1/2$, and $\omega = 2.5$,

$$H = p^2 - \tfrac{1}{2}\cos(\pi x) - \epsilon x \sin(\omega t). \tag{4}$$

The precise value of ϵ which effects the transition from regular to chaotic motion depends on the initial conditions as well as ω. In this paper we study the dynamics for initial conditions in the neighborhood of the point $(p_0, x_0) = (0.067\,14, -0.397\,00)$ for two values of ϵ, $\epsilon = 0.07$ and $\epsilon = 0.126$. For both of these values, the time dependent term can be considered a small perturbation on the cosine potential. In the first case, ($\epsilon = 0.07$), the classical motion is regular as evident from the fact that the motion is bounded for very long times ($t > 5000 \approx 1200$ cycles). In the second case, the motion of trajectories starting in this neighborhood is chaotic, becoming unbounded at $t \approx 20$. Being particularly unstable (by design), the midpoint trajectory, $x_t(p_0, x_0)$, is the first in the neighborhood to make its exit at $t \approx 14.5$. Our choices for the perturbation strength and initial conditions ensure that we are able to study the quantum evolution all the way up to the exit time without undue computational effort.

We pose the quantum problem in the semiclassical limit by setting $\hbar = 1/200\pi$. For this choice of $\hbar$, a typical quantum wavelength $\sqrt{\hbar/m\Omega} = 1/10\pi$, which is small compared to the scale of variation of the unperturbed potential. This permits us to start with a well-localized initial quantum state corresponding classically to a particle whose position and momentum are well known.

A. The quantum calculation

To study the quantum evolution, we propagate an initial wave function forward in time using a generalization to time-dependent Hamiltonians of the split exponential operator method of Feit, Fleck, and Steiger [16]. For a time-dependent potential, the $(\Delta t)^3$ dependence of the error in this method is preserved by replacing the potential-energy operator, $\hat{V}$, by its time average

$$\psi(t+\Delta t) = e^{-i\hat{T}\Delta t/2\hbar} e^{-i\int_{t_0}^{t_0+\Delta t}\hat{V}(t')\,dt'/\hbar} e^{-i\hat{T}\Delta t/2\hbar}\psi(t), \tag{5}$$

where $\hat{T}$ is the kinetic-energy operator. Our initial wave function, depicted schematically in Fig. 1(b), is a Gaussian wave packet centered at (p_0, x_0)

$$\psi(x,0) = (\pi\sigma^2)^{-1/4}\exp\left[-\frac{(x-x_0)^2}{2\sigma^2} + i\frac{p_0}{\hbar}(x-x_0)\right]. \tag{6}$$

The initial width σ is chosen so that the wave packet initially spreads as slowly as possible for motion in the unperturbed potential at the initial energy, $\langle H(t=0)\rangle = \langle H_0(p_0,x_0)\rangle = 0.3288$. In doing this we delay the Ehrenfest time as long as possible. Because the initial energy is well below the top of the well, the best choice for σ is only 3.4% larger than the width of the ground state wave function at the bottom of the cosine potential.

We include one cosine well on each side of the central well (three wells total) to allow for tunneling of the wave function out of the central well into the two adjacent wells. We set up the wave function across the three wells on a grid of 2048 points. Because the wave function must be represented on a finite grid, our computer simulation of the quantum problem breaks down as soon as the motion becomes unbounded. Thus we must limit our analysis to the times up to the moment that a large fraction of the wave function spills over the barrier from the central well to a neighboring well.

The resulting wave function $\psi(x,t)$ and its Fourier transform $\tilde{\psi}(p,t)$ are then used to compute $\langle x\rangle$, $\langle p\rangle$, and their variances $\langle(\Delta x)^2\rangle = \langle(\hat{x} - \langle\hat{x}\rangle)^2\rangle$ as a function of time. We also study the wave function directly by projecting it into the phase space. We will discuss how this is done in Sec. III D.

B. The classical calculation

The classical analog of the initial wave packet is a Gaussian probability distribution $\rho(x,p,t)$ with the same widths in position and momentum. The time evolution of this distribution is given by

$$\rho_{\rm cl}(p,x,t) = \int\int dp'\,dx'\,\delta(x - x_t(p',x')) \times\delta(p - p_t(p',x'))\,\rho_{\rm cl}(p',x',0), \tag{7}$$

where $x_t(p,x)$ and $p_t(p,x)$ represent the time-evolved phase-space coordinates as functions of the initial conditions.

We follow the behavior of the classical distribution by first generating 10 000 sets of initial conditions (x,p) distributed according to a two-dimensional Gaussian probability distribution centered at (x_0,p_0) and having the appropriate widths in position and momentum to match the initial quantum wave packet. We follow the time evolution of each "particle" in this cloud by integrating its classical equations of motion forward in time by a standard fourth order Runge Kutta algorithm.

The classical probability density at a given time may be depicted as a two-dimensional histogram of the time-evolved cloud. Using 10 000 points gives us a statistical error of roughly 10% for the one-dimensional histograms of Sec. IV assuming about 100 bins and a reasonably equi-

table distribution among the bins. We use this classical probability density to find $\langle x \rangle$, $\langle p \rangle$ and their variances $(\Delta x)^2$, $(\Delta p)^2$ from

$$\langle f \rangle_{\rm cl} = \int \int dp\, dx\, f(p,x)\, \rho_{\rm cl}(p,x,t), \tag{8}$$

to compare with their quantum analogs, and we also compare the reduced probability density $\rho_{\rm cl}(x,t) = \int dp'\, \rho_{\rm cl}(p',x,t)$ with the wave function $|\psi(x,t)|^2$.

C. The semiclassical calculation

For the semiclassical calculation we evolve the initial wave function forward in time using the semiclassical propagator of Van Vleck [17] and Gutzwiller [18]

$$\psi_{\rm sc}(x_{\rm f},t_{\rm f}) = \int dx'\, G_{\rm sc}(x_{\rm f},x';t_{\rm f})\, \psi(x',0) \tag{9}$$

with

$$G_{\rm sc}(x,x';t) = \sum_{\rm cl.paths} \left(\frac{1}{2\pi i\hbar}\right)^{1/2} \left|\frac{\partial^2 S(x,x',t)}{\partial x \partial x'}\right|^{1/2} \times \exp\left(i\frac{S(x,x',t)}{\hbar} - i\nu_t\frac{\pi}{2}\right) \tag{10}$$

where $S(x,x',t) = \int_0^t [p(t')\dot{q}(t') - H(p(t'),q(t'))]\, dt'$ is the cumulative classical action along a given classical trajectory $(q(t),p(t))$ and ν_t is the number of caustics [19] encountered on that trajectory, also known as the Gutzwiller phase. The sum in the above expression includes only those classical paths that begin at x' and end at x. The prefactor is the reciprocal square root of the determinant of the stability matrix and represents the Gaussian fluctuations about the classical path.

We evaluate the semiclassical wave function numerically using the cellular dynamics method of Heller and Tomsovic [20] by representing the propagator and the initial wave function as a sum of Gaussians in phase space and then linearizing the dynamics in the cell centered on each Gaussian. To implement this method, we must calculate the classical trajectories, the cumulative actions along those trajectories, and the time evolution of the stability matrix elements for a grid of initial conditions. If the width of our initial wave packet were small compared to a quantum wavelength, we would only need to compute the classical trajectories for a vertical strip of phase-space coordinates with different momenta at the location in $x = x_0$ of the center of the wave packet. This not being the case, we must include a grid of initial conditions in x as well as p. Even so, the initial wave packet is sufficiently localized that the central vertical strip still makes the primary contribution to the calculation, and the qualitative features of the semiclassical wave function may be found directly from the semiclassical propagator as though the initial wave function were a delta function.

The lattice spacings for the grid of initial conditions should be no larger than the cell dimensions, which should in turn be small compared to the characteristic quantum length and momentum, respectively. Because of the rapid divergence of paths having the same initial position and adjacent momenta, the momentum lattice spacing should actually be much smaller than the momentum cell dimension. Our rectangular grid of initial conditions consists of 31 grid points in x with a spacing of 0.011 14 and 1501 grid points in p with a spacing of 0.001 75. The widths of the Gaussians that define the cell dimensions are 0.011 14 and 0.017 50 in x and p, respectively. The span of the grid assures that the sums of Gaussians in x and p are approximately constant (meaning that the sums may be roughly approximated by integrals) and that the contributions of classical trajectories with initial momenta equal to the endpoint values are negligible.

D. Quantum phase-space transforms

In order to compare the quantum dynamics to the classical probability distribution, we must project the wave function into phase space. The two quantum phase-space transforms which are most commonly used for this purpose are the Wigner transform [21]

$$W(p,x) = \frac{1}{\pi}\int dy\, \psi^*(x-y)\, \psi(x+y) e^{2ipy/\hbar} \tag{11}$$

and the Husimi transform [22]

$$H(p,x) = |\langle p,x|\psi\rangle|^2 \tag{12}$$

where $|p,x\rangle$ is a coherent state. $W(p,x)$ has the desirable property that its projection onto the x and p axes gives the probability amplitudes $|\psi(x)|^2$ and $|\tilde{\psi}(p)|^2$, respectively. Not being positive definite, however $W(p,x)$ cannot be directly interpreted as a probability density. $H(p,x)$, on the other hand, is positive definite, but unlike $W(p,x)$, $H(p,x)$ cannot be directly projected onto the x and p axes to obtain $|\psi|^2$ and $|\tilde{\psi}|^2$ because the overlap of the coherent states blurs the information.

We have analyzed our results using both $H(p,x)$ and $W(p,x)$ and prefer the Husimi transform because we have found it considerably easier both to compute and to interpret. To assure ourselves that the features exhibited by $H(p,x)$ are not artifacts of the transform, we have compared $H(p,x)$ and $W(p,x)$, focusing on the nodal structure that develops after the equivalence time. In order to contour the sometimes negative and wildly oscillating Wigner transform, we first smoothed it by making a histogram of the transform and varied the bin size until the contouring program could make sense of it. We found that the nodes were clearly present in both transforms, giving us confidence that the features we observe using the Husimi transform are real.

IV. DISCUSSION OF RESULTS

As we mentioned in the Introduction, we observe three times which define stages in the development of the early time quantum dynamics for this system. These stages are characterized as localized classical behavior for $t < t_{\rm Eh}$,

delocalized classical behavior for $t_{Eh} < t < t_{eq}$, bounded nonclassical behavior for $t_{eq} < t < t_{ex}$, and unbounded nonclassical behavior for $t > t_{ex}$. The Ehrenfest time occurs when the expectation values of the position and momentum, $\langle x \rangle$ and $\langle p \rangle$, first differ from the classically-evolved coordinates of the center of the wave packet, $x_t(p_0, x_0)$ and $p_t(p_0, x_0)$, because of wave packet spreading. The equivalence time occurs when quantum observables like $\langle x \rangle$, $\langle x^2 \rangle$, and $|\psi|^2$ diverge from their classical counterparts because of quantum interference effects. Lastly, the exit time occurs when the dynamics become unbounded. The classical dynamics become unbounded when a non-negligible number of the 10 000 particles have left the central well. The quantum dynamics become unbounded when the probability amplitude spills over the barrier from the central well into a neighboring well. As tunneling is negligible under our conditions, the quantum exit time and classical exit time are the same. While we only present results for the behavior of the position and its variance, the behavior in momentum space is similar.

First, we consider the classically regular motion ($\epsilon = 0.07$). There is no exit time because this motion remains bounded, and for the time frame of our analysis ($t < 30$), there is no appreciable difference between the quantum and classical motion. Thus we observe only two stages in the early-time dynamics given by $t < t_{Eh}$ and $t > t_{Eh}$ with $t_{Eh} \approx 13$.

To show the delocalization of the wave packet that occurs at t_{Eh} we plot $\langle x \rangle$, $\langle x \rangle_{cl}$, and $x_t(p_0, x_0)$ as functions of time in Fig. 2(a). Note the divergence of $x_t(p_0, x_0)$ from $\langle x \rangle$ and $\langle x \rangle_{cl}$ at t_{Eh}. To further illustrate the spreading of the wave packet we plot in Fig. 2(b) the quantum and classical rms deviations, $\Delta x = \sqrt{\langle (x - \langle x \rangle)^2 \rangle}$, normalized to the halfwidth of the initial orbit. Note that

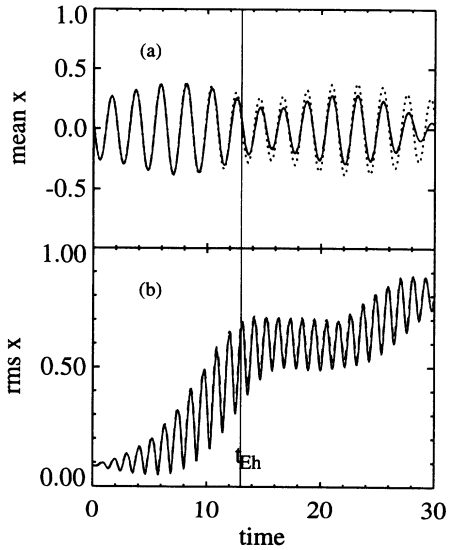

FIG. 2. (a) The quantum (solid) and classical (dashed) mean positions as functions of time compared to the classical evolution of the center of the wave packet (dotted) for $\epsilon = 0.07$. (b) The corresponding quantum (solid) and classical (dashed) rms deviations as functions of time normalized by the halfwidth of the initial orbit. The motion becomes delocalized at $t_{Eh} \approx 13$.

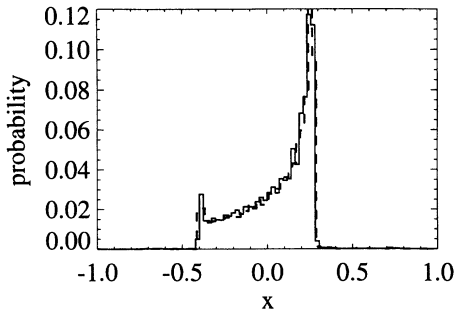

FIG. 3. A plot of the quantum (solid) and classical (dashed) probability densities as functions of x for $\epsilon = 0.07$ at $t = 25$.

this quantity is of order unity when the midpoint and mean trajectories diverge at t_{Eh}.

Figure 2(a) also shows that despite the spreading of the classical and quantum probability distributions, the quantum expectation values $\langle x \rangle$ and Δx are virtually indistinguishable from their classical counterparts. In fact we find that the classical and quantum distributions are essentially the same even after the distributions spread. To show this, we compare in Fig. 3 the quantum and classical probability densities at $t = 25$. To be fair in making this comparison we smooth the quantum data to match the resolution of the classical data by making a histogram of $|\psi|^2$ using the classical bin size. There is no discernible difference in the distributions save for statistical error in the classical distribution.

We now turn to the classically chaotic motion ($\epsilon = 0.126$). We already established in Sec. III that this motion becomes unbounded at $t_{ex} \approx 14.5$. In Fig. 4 we show

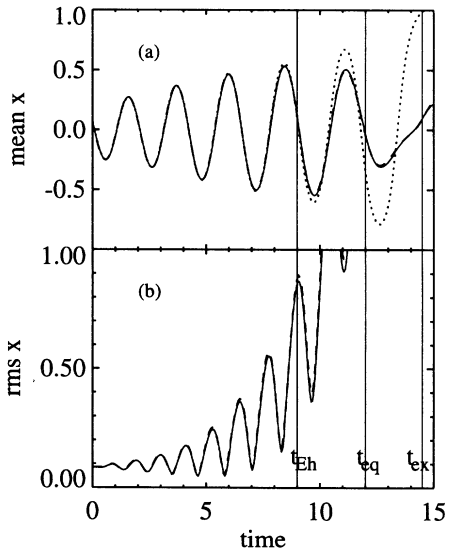

FIG. 4. (a) The quantum (solid) and classical (dashed) mean positions as functions of time compared to the classical evolution of the center of the wave packet (dotted) for $\epsilon = 0.126$. (b) The corresponding quantum (solid) and classical (dashed) rms deviations as functions of time normalized to the halfwidth of the initial orbit. The motion becomes delocalized at $t_{Eh} \approx 9$ and unbounded at $t_{ex} \approx 14.5$.

the delocalization of the wave packet in the same manner as for $\epsilon = 0.07$. Note the departure of the central trajectory from the mean and the accompanying growth of the rms deviation(s), as before. We see that the wave packet spreads more rapidly than for the classically regular motion with $t_{\mathrm{Eh}} \approx 9$.

Unlike the classically regular motion, we observe a subtle but appreciable difference in the dynamics beginning at $t_{\mathrm{eq}} \approx 12$ that is not apparent from the expectation values in Fig. 4. To illustrate this, we compare the quantum and classical probability densities before and after t_{eq}. These comparisons are shown in Figs. 5(a) for $t = 11$ and 5(b) for $t = 13$. As before, we smooth the quantum data to match the classical resolution. Note the difference in the fine structure of the two distributions for $0 < x < 0.5$.

While the phenomenon of wave-packet spreading is typically thought of as a manifestation of quantum dynamics, for our problem its origin is really classical. The fact that t_{Eh} occurs sooner for $\epsilon = 0.126$ ($t_{\mathrm{Eh}} \approx 9$) than for $\epsilon = 0.07$ ($t_{\mathrm{Eh}} \approx 13$) reflects the greater sensitivity of the classical dynamics to the initial conditions for the former. At these very early times, the divergence of the classical trajectories is directly reflected in the spreading of the quantum wave packet. Moiseyev and Peres [23] also observed greater rates of spreading for quantum wave packets launched in the chaotic regions compared to the regular regions of the Henon-Heiles potential.

Given the work of Berry *et al.* [8] and of Sepulveda *et al.* [12] discussed in the Introduction, one would expect the accuracy of semiclassical dynamics to persist longer for $\epsilon = 0.07$ than for $\epsilon = 0.126$ because the regular classical behavior of the former is governed by an elliptic fixed point of the unperturbed motion while the chaotic classical behavior of the latter is governed by the hyperbolic fixed points. While we do not directly address this question, we do observe that the equivalence of the quantum and classical dynamics persists much longer for $\epsilon = 0.07$ ($t_{\mathrm{eq}} > 30$) than for $\epsilon = 0.126$ ($t_{\mathrm{eq}} \approx 12$). The chaotic motion feels the effects of the quantum mechanics sooner than the nonchaotic motion. Thus we would expect that chaotic motion would feel the higher order nonsemiclassical effects of quantum mechanics sooner as well.

Having established the stages of the dynamics for $\epsilon = 0.126$ given by $t_{\mathrm{Eh}} < t_{\mathrm{eq}} < t_{\mathrm{ex}}$, we focus on the times surrounding $t_{\mathrm{eq}} \approx 12$ in order to discuss the role of the underlying classical phase-space structures in the onset of the nonclassical behavior. In Figs. 6, 7, and 8 we show the classical, quantum, and semiclassical phase-space portraits before, during, and after the breakdown of the quantum-classical equivalence at $t = 11$, $t = 12$, and $t = 13$, respectively. The classical phase-space distributions are depicted as dot plots in Figs. 6(a), 7(a), and 8(a) where each dot represents the time-evolved coordinates of one of the 10 000 particles. The quantum and semiclassical Husimi transforms are depicted as contour plots in Figs. 6, 7, and 8. The contour plot level spacings are on a log scale with gray being low and black being high.

The folded structure which appears in the classical distribution after $t \approx 12$ [see Fig. 7(a) and Fig. 8(a)] is a manifestation of the chaotic dynamics. These folds are

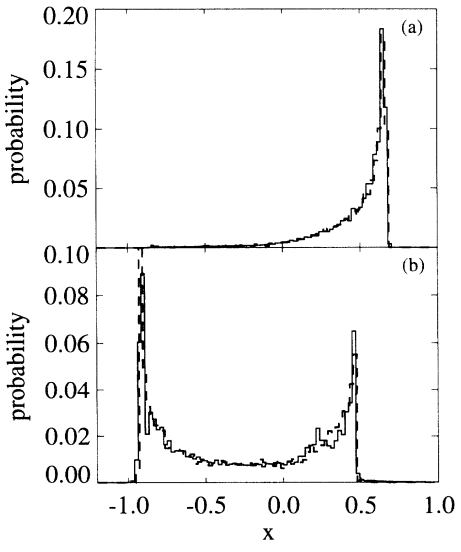

FIG. 5. A comparison of the quantum (solid) and classical (dashed) probability densities as functions of x for $\epsilon = 0.126$ at (a) $t = 11$ and (b) $t = 13$. In the latter, the quantum distribution has acquired oscillations (see $0.5 < x < 1.0$) that are absent from the classical distribution.

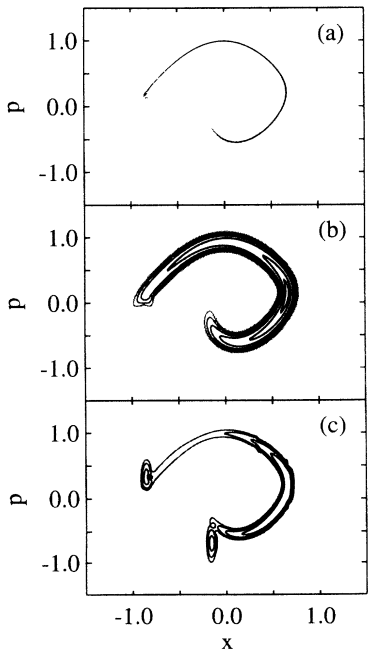

FIG. 6. A comparison of the classical, quantum, and semiclassical phase-space portraits for $\epsilon = 0.126$ at $t = 11$. (a) The 10 000 time-evolved phase-space coordinates of the classical distribution. (b) The Husimi transform of the wave function. (c) The Husimi transform of the semiclassical approximation to the wave function. The level spacings for the contour plots in (b) and (c) are on a $\log_{10}$ scale. The classical phase-space structure which characterizes this motion is a whorl.

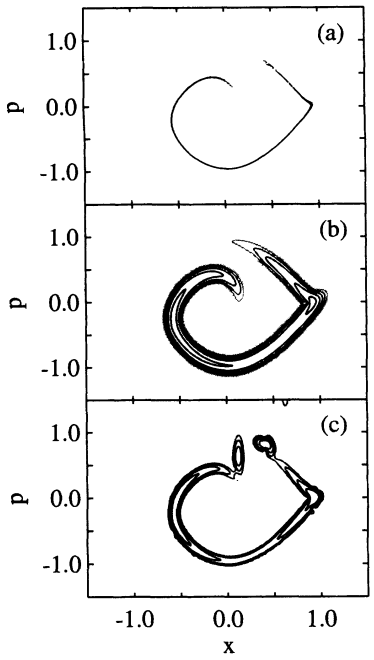

FIG. 7. A comparison of the classical, quantum, and semiclassical phase-space portraits for $\epsilon = 0.126$ at $t = 12$, similar to that of Fig. 6. The classical distribution is on the verge of being folded by the hyperbolic fixed point to produce a tendril.

essentially equivalent to the tendrils of Berry *et al.* which characterize the development of chaos around unstable fixed points in conservative systems. For our particular choice of initial conditions, there are two folding events prior to the exit time at $t \approx 12$ and $t \approx 13.5$, and a third folding event coincident with the exit time at $t \approx 14.5$. Leading up to the first folding event, the classical probability density becomes concentrated along the remnant of the $\epsilon = 0$ separatrix. The folds in the distribution subsequently emerge after approaching the hyperbolic fixed point. While neither the separatrix nor the hyperbolic fixed points are clearly defined, even in a KAM sense, it appears that the remnants of these structures still govern the motion. In the subsequent discussion we use these terms for lack of any better.

The primary result of our analysis concerns the nodes which appear in the quantum phase-space distribution when the classical probability density exhibits the folding associated with the classical chaos. Because the nodes are clearly present in both the quantum and semiclassical pictures [cf. Fig. 8(b) and Fig. 8(c)], their origin must be semiclassical. To discuss the origin of the nodes in greater detail, we magnify the folded/nodal structure of Fig. 8. We plot in Figs. 9(a) and 9(b) the quantum and semiclassical phase-space transforms on top of the classical dots in order to show the locations of the nodes in relation to the classical phase-space structure.

While the reproduction of the nodal structure by the semiclassical calculation shown in Fig. 9(b) is clearly imperfect, the qualitative agreement is apparent. It is difficult to get better agreement for this fine structure because the grid of initial conditions gets drastically stretched by the dynamics, especially after the folding process begins, resulting in intervals along the classical

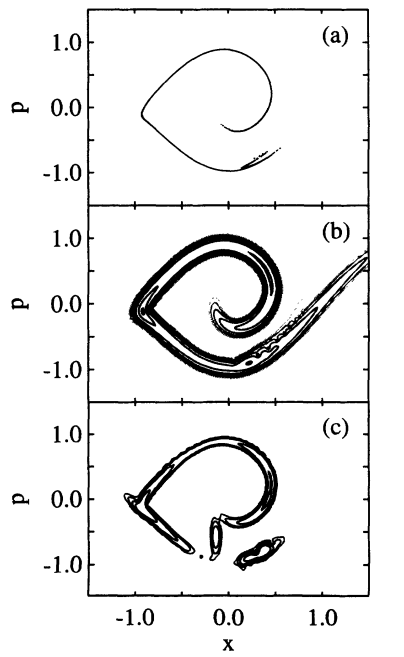

FIG. 8. A comparison of the classical, quantum, and semiclassical phase-space portraits for $\epsilon = 0.126$ at $t = 13$, similar to that of Fig. 6 and Fig. 7. The quantum transform has acquired a nodal structure for which the underlying classical structure is a tendril.

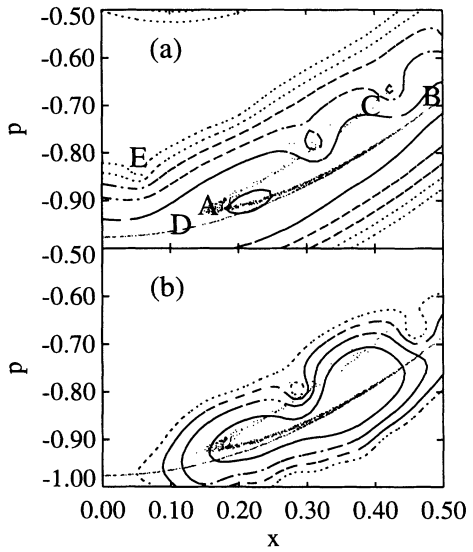

FIG. 9. (a) An enlargement of the nodes in Fig. 8(b) plotted with the classical distribution to show the locations of the nodes in relation to the classical structure. The coordinates (x, p) of the two nodes shown are $(0.39, -0.80)$ and $(0.42, -0.69)$. (b) The same plot for the semiclassical approximation of Fig. 8(c). In (a) the levels are -3.5, -4, -5, -6, -7, and -8 while in (b) the levels are -3.5, -4, -4.5, and -5. In both cases the spacings are on a $\log_{10}$ scale with solid being high and dotted being low. The letters (A–E) in (a) are for reference in the discussion.

distribution where the paths become too sparsely represented to get the nodes in precisely the right places. The agreement does improve by increasing the density of the grid of initial conditions, particularly the vertical (momentum) grid density; however, the computation time also increases linearly with the total number of grid points, thereby preventing any substantial improvement over the results we present given our computational constraints. The spurious peaks associated with caustics also impede agreement between the quantum and semiclassical pictures. As these peaks appear because there really are poles at the caustics in the semiclassical propagator, they cannot be eliminated. In particular, the false amplitude associated with these poles reduces the amplitude associated with the real features in the wave function. Given these problems and the subtle nature of the nonclassical features in the quantum transform, it is not surprising that the semiclassical calculation can only reproduce the two most prominent nodes.

The snapshots in time of the classically evolved cloud in Figs. 6(a), 7(a), and 8(a) may be interpreted as a flow field that is stretched and compressed in accordance with the underlying KAM orbit structure. Note that the general sense of the flow is clockwise. This is reflected by the sense of the change in the cumulative action which increases in the direction of flow for $p\,dx > 0$ and decreases in the direction of flow for $p\,dx < 0$. Also note that the classical amplitude piles up at the "turning points" where the distribution is locally vertical in (x,p). Strictly speaking, this interpretation is only valid locally, i.e., for flow times which are short compared to the period of the perturbation. Thus one may interpret short segments of the flow which have the same initial and final positions as classical paths that should interfere in the semiclassical sense. In particular, we find that the flow segments CA and BD of Fig. 9(a) are interfering with one another to produce the observed nodal structure.

As previously explained in Sec. III C, the qualitative features of the semiclassical wave function may be inferred directly from the semiclassical propagator $G_{\rm sc}(x,x_0,t)$. The latter being simply a sum of complex terms, each having an amplitude and a phase, we approximate the wave function at $x = x_{\rm f}$ and $t = t_{\rm f}$ as $\psi_{\rm sc}(x_{\rm f},t_{\rm f}) \approx \sum A_{\rm sc} \exp(i\phi_{\rm sc})$ where the phase associated with a given path is $\phi_{\rm sc}(x_{\rm f},x_0) = S(p_0,x_0,t)/\hbar - \nu_t\pi/2$ and the amplitude, which is essentially a measure of the path density, is $A_{\rm sc} \sim |\partial x_{\rm f}/\partial p_0|^{-1/2}$. In order for there to be discernible interference among the terms in the propagator, their relative phases must not vary too rapidly (or else the interference term vanishes under the integral which we are suppressing), and their amplitudes must not be too dissimilar. Assuming these conditions are satisfied, the locations of the nodes in the wave function can be inferred given the number of terms involved, their relative phases, and their relative magnitudes.

If we examine the relative phases for the paths AB, CA, and BD of Fig. 9(a), we find that the phases of paths BD and CA differ by π at the locations (in x) of the nodes. We also find that this phase difference varies at a rate which correctly accounts for the spacing of the nodes. In particular, the rate of variation of the phase difference for paths BD and CA is about seven cycles per unit length in contrast to the 50-fold greater rates of variation for paths BD and AB and for paths AB and CA.

The positions of the nodes can be deduced from the semiclassical amplitudes for the two interfering paths. The relative amplitudes of the two interfering paths are indicated by the classical dot densities of Fig. 9. If the dot densities for the interfering paths were equal, then we would expect the nodes to be centered (in p) between them. In Fig. 9 we see that the dot density for path BD is at least 10 times greater than the dot density for path CA. As a result, the node centers (where the destructive interference is complete) are pulled off center toward the path of lower amplitude.

The only places where our flow-field interpretation is wrong is at the turning points associated with the folded structure [points A, B, and C in Fig. 9(a)]. By tracking the caustic counts for the particles which comprise the flow, we found that the caustic count decreases by one rather than increasing by one at the nose of the fold (point A). Because the caustic count can only increase with time, the flow must be discontinuous at points B and C as well as at point A making all three of these points spurious caustics in the flow field. As a result, the Gutzwiller phases for the two interfering paths (CA and BD) are the same because the caustic that is lost at point A is "subsequently" found at point B.

Because the flow-field interpretation of the classical probability density is locally valid (except at the three spurious caustics) and because the Gutzwiller phases for the two interfering paths are the same, the phase-space area enclosed by the interfering paths between successive nodes should be $\approx 2\pi$. The 2π phase difference between beats is given by

$$\phi_1 - \phi_2 = \int_{x_n}^{x_{n+1}} [p_1(x) - p_2(x)]/\hbar \, dx + \delta, \qquad (13)$$

where x_n and x_{n+1} are the positions of the successive nodes and $\delta = \int [V_t(x_2,t) - V_t(x_1,t)]\,dt/\hbar$ is the phase change due to the time varying piece of the Hamiltonian. If δ were zero the phase-space area given by the first term should be equal to 2π. The measured area enclosed by paths BD and CA of Fig. 9(a) between the two dominant nodes is ≈ 6.2. As an order of magnitude estimate, we find that $|\delta| \sim \epsilon(\Delta p)T/\hbar\omega$ where Δp is the momentum difference between the paths and T is the time difference between beats. For $\Delta p \approx 0.08$ and $T \approx 0.06$ we find that $\delta \sim 0.15$, so the phase difference between the nodes is roughly consistent with 2π.

Besides the nodal structure, we observe a slight pinch in the quantum phase-space distribution at the leading edge of the nose of the fold, located at point E in in Fig. 9(a). Like the nodes, the pinch forms when the classical probability distribution acquires the tendrils associated with motion near a hyperbolic fixed point. Unlike the nodes, however, the pinch cannot be explained as an interference phenomenon as there are no underlying classical paths at the pinch to interfere. This absence of underlying classical structure suggests that the pinch does not have a semiclassical origin, but rather arises from quantum fluctuations around the classical paths. Un-

fortunately, our semiclassical calculation does not have sufficient resolution to verify this supposition.

V. CONCLUSIONS

We find that the quantum and classical pictures are equivalent (within the limitations of our statistics) well beyond the Ehrenfest time. Thus we see that being in the classical limit does not necessarily mean that the dynamics must be localized. We also find that this quantum-classical equivalence persists much longer in the absence of classical chaos. We conclude that for the wave packet to remain localized beyond the equivalence time, which is when the phase-space structures of the classical chaos first appear, $\hbar$ must be much smaller than our choice of $1/200\pi$. This would mean a quantum length scale which is negligibly small compared to the scale of variation of the potential.

We know that the repeated folding of the classical probability density that results from the flow interacting with the hyperbolic fixed points is the mechanism which eventually spreads the classical amplitude uniformly throughout phase space, bringing about the mixing behavior that characterizes chaos. We find that this same mechanism also results in the breakdown of the quantum-classical equivalence that characterizes the early-time dynamics of our system in the absence of classical chaos. Specifically, we find that the quantum phase-space transform exhibits a nodal structure on top of the tendrils that result from the classical folding process. We have shown that the contributions to the semiclassical propagator by those tendrils which have the same Gutzwiller phases differ in phase by π at the locations (in x) of the quantum nodes. We have also shown that the variations of the phase difference between the tendrils correctly accounts for the spacing between the nodes and that the relative amplitudes of the tendrils correctly accounts for their locations (in p).

The development of these nodes as a result of tendrils beating against one another is a concrete example of how quantum interference, by punching holes in the classical probability density, inhibits classical mixing. Because of the essential role played by tendrils (and the underlying hyperbolic fixed points) in the onset of classical chaos, we would expect these nodes to be a generic feature in quantum chaotic dynamics which contributes to the quantum suppression of mixing. We would also expect interference of this nature—between classical paths having nearby origins in phase space—to be the dominant effect while the motion remains bounded; but other quantum interference effects—involving classical paths with distant origins or nonclassical paths, for examples—may become important as the classical chaos becomes more fully developed.

In addition to the nodal structure, we find that the quantum phase-space distribution acquires a slight pinch at the leading edge of the nose of the fold. The absence of classically folded structure underlying the pinch suggests that its origin is probably not semiclassical. Regardless of its origin, the pinch, like the nodes, contributes to the inhibition of classical mixing by redistributing the classical probability amplitude.

ACKNOWLEDGMENTS

We would like to thank E. Heller, S. Tomsovic, M. Sepulveda, and W. Lin for useful discussions. This work was supported by the National Science Foundation under Grant No. DMR–9020310.

[1] T. Hogg and B. A. Huberman, Phys. Rev. Lett. **48**, 711 (1982); Phys. Rev. A **28**, 22 (1983).
[2] M. V. Berry and M. Tabor, Proc. R. Soc. London **356**, 375 (1977); for a recent comprehensive review, see O. Bohigas, S. Tomsovic, and D. Ullmo, Phys. Rep. **223**, 43 (1993) and references therein.
[3] R. L. Waterland, J. Yuan, C. C. Martens, R. E. Gillilan, and W. P. Reinhardt, Phys. Rev. Lett. **61**, 2733 (1988).
[4] E. J. Heller, Phys. Rev. Lett. **53**, 1515 (1984); E. J. Heller, in *Chaos and Quantum Physics*, edited by M. J. Giannoni, A. Voros, and J. Zinn-Justin, Les Houches Session LII, 1989 (Elsevier, Amsterdam, 1991); S. Tomsovic and E. J. Heller, Phys. Rev. Lett. **70**, 1405 (1993).
[5] Y. B. Zel'dovich, Zh. Eksp. Teor. Fiz. **24**, 1006 (1967) [Sov. Phys. JETP **24**, 1006 (1967)].
[6] W. A. Lin and L. E. Reichl, Phys. Rev. A **37**, 3972 (1988).
[7] R. Scharf and B. Sundaram, Phys. Rev. A **45**, 3615 (1992).
[8] M. V. Berry, N. L. Balaza, M. Tabor, and A. Voros, Ann. Phys. (N.Y.) **122**, 26 (1979).
[9] S. Tomsovic and E. J. Heller, Phys. Rev. Lett. **67**, 664 (1991).
[10] S. Tomsovic and E. J. Heller, Phys. Rev. E **47**, 282 (1993).
[11] P. W. O'Connor and S. Tomsovic, Ann. Phys. (N.Y.) **207**, 218 (1991); P. W. O'Connor, S. Tomsovic, and E. J. Heller, Physica D **55**, 340 (1992); J. Stat. Phys. **68**, 131 (1992).
[12] M. A. Sepulveda, S. Tomsovic, and E. J. Heller, Phys. Rev. Lett. **69**, 402 (1992).
[13] W. A. Lin and L. E. Reichl, Phys. Rev. A **31**, 1136 (1985).
[14] B. V. Chirikov, Phys. Rep. **52**, 263 (1979).
[15] M. C. Gutzwiller, *Chaos in Classical and Quantum Mechanics* (Springer, Berlin, 1990), Chap. 9.
[16] M. D. Feit, J. A. Fleck, Jr., and A. Steiger, J. Comp. Phys. **47**, 412 (1982).
[17] J. H. Van Vleck, Proc. Natl. Acad. Sci. USA, **14**, 178 (1928).
[18] M. C. Gutzwiller, J. Math. Phys. **8**, 1979 (1967).
[19] A trajectory, $x_t(p_0, x_0)$, encounters a caustic whenever $\partial x_t/\partial p_0$ changes sign. In one dimension a caustic is equivalent to a turning point.
[20] E. J. Heller, J. Chem. Phys. **94**, 2723 (1991).
[21] E. Wigner, Phys. Rev. **40**, 749 (1932).
[22] K. Husimi, Proc. Phys. Math. Soc. Jpn. **22**, 264 (1940).
[23] N. Moiseyev and A. Peres, J. Chem. Phys. **79**, 5945 (1983).